



# Petrology, mineralogy, and geochemistry of the olivine diogenite NWA 4255: new insights into the magmatic evolution of asteroid 4 Vesta

Ratiba Kared<sup>1</sup> · Bertrand N. Moine<sup>2</sup> · Abdelmadjid Seddiki<sup>1</sup> · Jean Yves Cottin<sup>2</sup> · Richard C. Greenwood<sup>3</sup> · Ian A. Franchi<sup>3</sup>

Received: 18 January 2019 / Accepted: 5 July 2019  
© Saudi Society for Geosciences 2019

## Abstract

Northwest Africa (NWA) 4255 is a meteorite found in the region of Tindouf (southwestern Algeria), classified as brecciated olivine diogenite. Based on textural observations and orthopyroxene compositions, two different lithologies were determined: harzburgitic and orthopyroxenitic. The orthopyroxenitic lithology contains orthopyroxene (Mg no. 73.99–75.68) and spinel (Cr no. 83.09–85.11, Mg no. 15.57–22.45). On the other hand, the harzburgitic lithology contains orthopyroxene (Mg no. 74.54–77.14) and olivine (Mg no. 70.94–72.57). The iron metal and the sulfides (Troilites) of this sample are present in both lithologies and are low in Ni (Ni < 0.1 wt%). The Fe/Mn ratio of orthopyroxenes ranges from 22.28 to 32.64 and show a large overlap between both lithologies. Lowest ratios are unusual; they are below the defined field for diogenites and olivine diogenites.  $\Delta^{17}\text{O}$  values are  $-0.234 \pm 0.003$  (1 $\sigma$ ) and confirm that the NWA 4255 originated from 4Vesta. The results of this study show that there is a genetic linkage between the two lithologies of NWA 4255 and correspond to in situ crystallization processes. This olivine diogenite reflects transition between two major magmatic processes in 4Vesta. The magma ocean of 4Vesta crystallized at equilibrium, allowing the formation of a dunitic and harzburgitic mantle. This late lithology is linked to the peritectic reaction between the olivines formed and the evolved liquid. Our sample then reflects this crucial step of separating this mantle from the residual liquid. This melt evolving on the peritectic allowed the formation of the observed harzburgitic assemblage and then evolves out from the peritectic reaction to proceed to a fractional crystallization process involving the formation of orthopyroxenite.

**Keywords** NWA 4255 · Olivine diogenite · Harzburgite · Orthopyroxenite · Peritectic reactions · 4Vesta

---

Editorial handling: Domenico M. Doronzo

**Electronic supplementary material** The online version of this article (<https://doi.org/10.1007/s12517-019-4604-9>) contains supplementary material, which is available to authorized users.

✉ Abdelmadjid Seddiki  
abdelmadjid.seddiki69@gmail.com

- <sup>1</sup> Laboratoire Géoressources et Risques Naturels (GEOREN); Oran2 University, BP: 1510, 31000 Oran, Algeria
- <sup>2</sup> Magmas & Volcanoes Laboratory UMR6524 CNRS, Lyon University, UJM, Saint-Etienne, France
- <sup>3</sup> Planetary and Space Sciences, Department of Physical Sciences, The Open University, Walton Hall, Milton Keynes MK7 6AA, UK

## Introduction

The HED (Howardite, Eucrite, Diogenite) group of meteorites likely originated from the Asteroid 4Vesta (Drake 2001). Diogenites are predominantly orthopyroxene-rich cumulates (Krawczynski et al. 2008; Mandler and Elkins-Tanton 2013). However, recently, olivine diogenites have been recognized as an important subset of diogenites and are considered to represent the most primitive material within this subgroup (Krawczynski et al. 2008). The designation olivine diogenite has been used for diogenites containing a considerable range of modal olivine contents, from trace to 50 wt.% olivine (Bowman et al. 1997; Irving et al. 2009; Mittlefehldt 1994; Sack and Ghiorso 1991; Shearer et al. 2010). However, when the olivine abundance is between 1 and 5%, the most appropriate term is olivine-bearing diogenites (Shearer et al. 2010). Diogenites, olivine-bearing diogenite, and olivine diogenites are petrogenetically associated with basaltic magmatism linked to

the earliest stages of asteroidal melting on the parent body of the Howardite–Eucrite–Diogenite (HED) meteorites (Shearer et al. 2010). As pointed out by Mittlefehldt (2000), the origin of the parental magmas of diogenites remains poorly understood.

In this study, we look in detail at the origin and interrelationship between two distinct lithologies present in the olivine diogenite NWA 4255. We examine the major processes responsible for their genesis using petrology, mineral chemistry, and whole-rock geochemistry. In particular, we examine whether the two lithologies are co-genetic. Using the evidence from modeling studies, we investigate the relationship between diogenites and olivine diogenites and assess how NWA 4255 fits into the magmatic history of 4Vesta. Finally, we use the information gained from this detailed study of NWA 4255 to examine the differentiation and crystallization history of vestian magma ocean.

## Petrography and texture

NWA4255 is an olivine diogenite discovered in 2002 in the Algerian Sahara. It is in the form of many fragments (Fig. 1a) totaling a mass of 6 kg. Some fragments show a thin fusion crust. Iron oxide is observed on some fragments, which reflects a supergene alteration of iron metal. The study concerns seven fragments of this meteorite. NWA4255 is a brecciated olivine diogenite. Observations under optical microscope (reflected light) and electron microscope allowed to highlight the presence of two lithologies, one contains olivine and is designated here as being the “harzburgitic lithology,” and the other is olivine free and is designated here as being the “orthopyroxenitic lithology.” Iron metal and sulfides are present in small amounts as interstitial grain or tiny inclusions in orthopyroxene. Clinopyroxene is present as traces associated with iron metal within large orthopyroxene grains. The “orthopyroxenitic lithology” consists of orthopyroxene, spinel, sulfide, and scarce clinopyroxene (see below) (Figs. 1 and 2). This olivine diogenite consists of orthopyroxene (91.62%), olivine (6.79%), chromium spinel (1.08%), and trace of sulfide and iron metal.

One of the most interesting features of the NWA 4255 is the presence of many small vugs in orthopyroxene and occasionally in the spinel in the orthopyroxenitic lithology. These vugs are associated with strings of sulfide and spinel inclusions (Fig. 1b, c).

## Orthopyroxenitic lithology

### Orthopyroxene

Orthopyroxene occurs as subhedral grains exhibiting a wide range of sizes (~8 to 0.01 mm in length) (Fig. 1d). In most cases, these grains are highly brecciated and are presumably fragments of much larger crystals. The original magmatic

boundaries between orthopyroxene and spinel are sometimes preserved. In addition, clinopyroxene is also present and occurs as very small grains (~50 μm). It is associated with iron metal in orthopyroxene.

### Chromium spinel

Spinel has several habitus and microstructures. Most spinels occur as subhedral to anhedral grains with a size of 100 to 600 μm. These spinel grains are highly brecciated when they are within or in contact with orthopyroxene (Fig. 1e). However, some spinels are euhedral (300 to 550 μm in diameter) showing igneous contacts with orthopyroxene (Fig. 1f). In addition, some small spinel grains are associated with sulfides (Fig. 2a). These grains often display curved contacts with orthopyroxene grains. Furthermore, there are spinels that form tiny inclusions (< 10 μm) and are associated with numerous vugs and sometimes with sulfides along cleavage planes within orthopyroxene grains.

### Sulfides

Sulfides are more abundant in the orthopyroxenitic lithology. They are less common in the harzburgitic lithology. The shape and the grain size of sulfides are largely variable; some are subhedral (~360 μm in diameter) (Fig. 2b). Others are euhedral (20 to 50 μm), and most were observed as tiny grain inclusions within orthopyroxene and spinel.

## Harzburgitic lithology

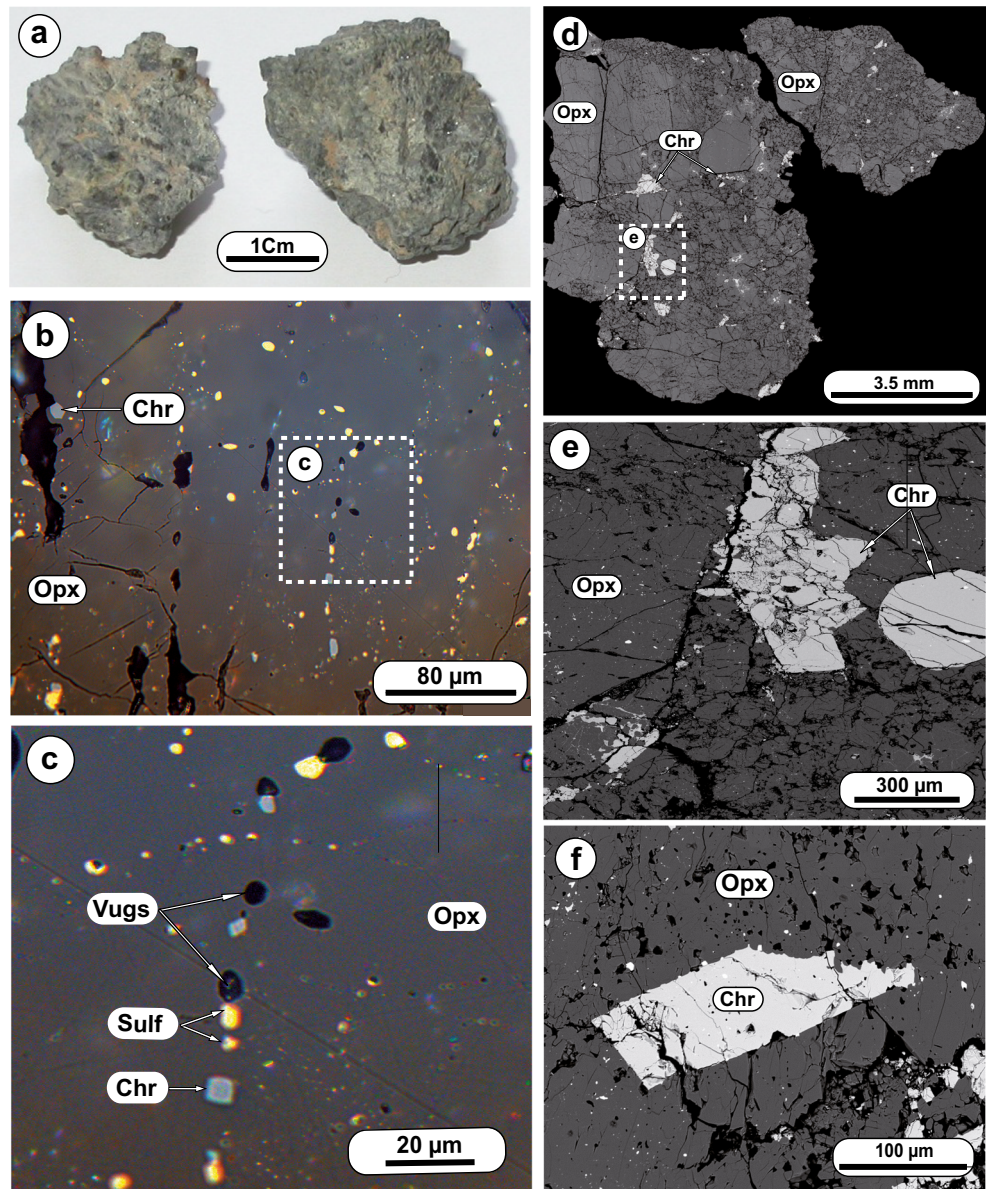
### Orthopyroxene

Orthopyroxenes are essentially subhedral, varying in size to 2 mm to 1.5 cm in the longest dimension (Fig. 3a). Most orthopyroxene grains are fractured and contain numerous olivine, chromium spinel, iron metal, and sulfide inclusions. In brecciated areas, pyroxenes are small and display angular shapes, and range in size from 10 to 250 μm. There are some orthopyroxenes found exceptionally as inclusions in olivine. These orthopyroxenes can be up to 200 μm in longest dimension; they are anhedral with irregular boundaries (Fig. 3b and c).

### Olivine

Olivine occurs only in harzburgitic lithology. It displays a heterogeneous distribution occurring as millimeter-sized fragmented crystals, locally displaying original contacts with orthopyroxene grains. Olivine grains are anhedral, ranging in size from 250 μm to 1.5 mm (Fig. 3a).

**Fig. 1** **a** Two of many fragments of NWA 4255. **b, c** Optical microscope photomicrographs observed in reflected light showing small vugs associated with strings of sulfides (Sulf) and chromium spinels (Chr) are common in the orthopyroxene (Opx) groundmass. **d** Mosaic backscattered electron (BSE) image of orthopyroxenitic lithology of studied sample, formed by orthopyroxenes and chromites. **e** Backscattered electron image of brecciated zone of NWA 4255 displaying two different types of chromium spinel, one is subhedral exhibiting irregular fractures and another is euhedral, and both are surrounded by an orthopyroxene breccia. **f** Euhedral chromium spinel within large orthopyroxene



Some small rounded grains of olivine (25–70 μm) are occasionally found as inclusions within large orthopyroxenes (Fig. 3e and f).

**Iron metal**

Iron metal is not abundant in NWA 4255, occurring as irregularly shaped grains associated with orthopyroxene and

**Fig. 2** Optical microscope photomicrographs observed in reflected light of anhedral chromites (Chr) associated with euhedral sulfide (Sulf) inclusions within orthopyroxene (Opx) in **a**, and euhedral sulfide showing contact angle within orthopyroxene in **b**

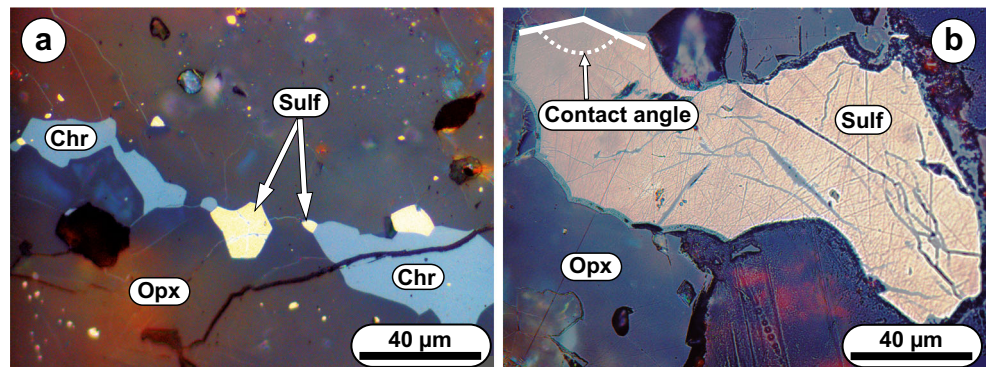
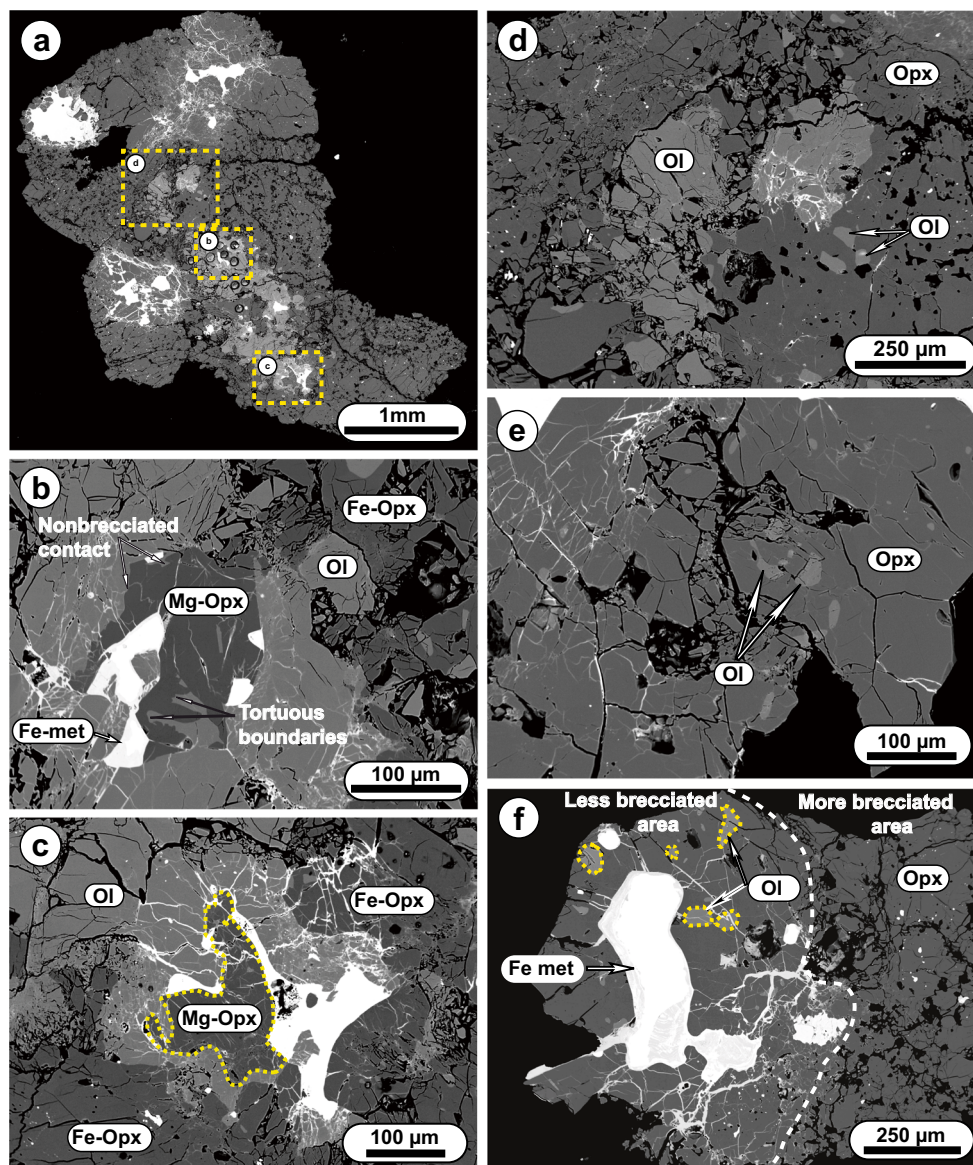


**Fig. 3** Backscattered electron (BSE) images showing textures and grain sizes of minerals found in the harzburgitic and transitional lithologies of NWA 4255. **a** Mosaic image of a brecciated fragment with large grains of olivine and iron metal. **b, c** Magnesian orthopyroxene associated with an iron metal (Fe met) inclusion in a large olivine grain (Ol). Note that the contact between orthopyroxene and olivine grains is usually non-brecciated. **d** BSE image of olivine-rich zone showing a close-up view of the square area indicated in **a**. **e, f** BSE images; showing some rounded olivine inclusions in orthopyroxene in **e**. Olivine and large iron metal grains within less brecciated orthopyroxene. Orthopyroxene and tiny small iron metal grain occur in more brecciated areas in **f**



sometimes with olivine. The iron grains can be as much as 500 µm in diameter; these larger grains (Fig. 3f) have a halo of infiltrations in cracks of surrounding orthopyroxene and olivine. Metallic iron is also in the form of very small grains (less than 10 µm), associated with sulfides and spinels in the form of trails of inclusions in orthopyroxene.

### Analytical techniques

Analyses of major and trace elements in various mineral phases were carried out using the electron microprobe and by LA-ICP-MS (laser-ablation inductively coupled plasma mass spectrometer). Image of the rock fragment presented in this work is a mosaic image corresponding to an accumulation of 28 images obtained using a scanning electron microscope

(Jeol JSM-5910 LV) equipped with a PGT Spirit microanalysis system. Whole-rock major and trace element analysis and oxygen isotope analyses were undertaken on two fresh fragments of NWA 4255 weighing 1.56 g and 1.57 g (Aliquot 1 and Aliquot 2). These were crushed and pulverized in an agate mortar before determining the concentrations of the major and trace elements of the whole rock.

### Mineral phases major and trace element analyses

Major and minor element chemistry of mineral phases was determined using an electron microprobe (CAMECA S×100, 15 kV, 20 nA), at Magmas and Volcanoes laboratory (LMV)–Clermont-Ferrand-France. Standards were natural

and synthetic minerals; ZAF corrections were applied. The limit of detection of the electron microprobe analyses is LOD = 50–100 ppm depending on the element concerned.

Trace element compositions were acquired by a LA-ICP-MS (laser-ablation inductively coupled plasma mass spectrometer) at the LMV, France, using a RESONETICS RESOLUTION M-50 laser powered by an ultra-short pulse ATL ATLEXEXCIMER laser system. Operating conditions were of 193 nm wavelength, 73  $\mu\text{m}$  spot diameter, associated to a repetition rate of 6 Hz. The sample was ablated in a He atmosphere using a 193-nm wavelength laser computer-controlled and equipped with an ATL laser with ultra-short pulse duration (< 4 ns). Acquisition time was 90 s for background and 60 s for signal. The international standards NIST612 and BCR2 (Columbia River Basalt) were used as external calibration standards. Four analyses were performed on these standards before and after each data collection set. Si and Cr determined by electron microprobe are used as internal standards to normalized concentration. The detection limits of all the elements analyzed are less than 1 ppb. Reproducibility and accuracy of the analyses was estimated through repeated analyses of BCR-2g standard at the beginning and at the end of every run. Data reduction was carried out using the software package GLITTER (Van Achterberg et al. 2001). For each analysis, the time resolved signal for each element was monitored to discard perturbations related to inclusions, fractures or mixing.

## Whole-rock major and trace element analyses

Two different techniques were used for major elements analysis. As for the first, a powdered sample (108 mg) of the Aliquot 1 was taken, from which a small fraction (about 5 mg) was deposited on a platinum wire and heated to 1580 °C in air. The molten glass was quenched in water. The glass beads obtained were then analyzed by electron microprobe. These glass beads were prepared at the CRPG-Nancy-France, and then analyzed by electron microprobe at the LMV-France. In this work, we present the average of three analyses that were made on each three beads made.

For the second technique, 100 mg of both aliquots (1 and 2) were taken to perform the major element analyses using the alkaline fusion method with  $\text{LiBO}_2$  (1:3 dilution). One hundred milligrams of each extracted powder was mixed with 300 mg of lithium metaborate ( $\text{LiBO}_2$ ). The mixture was then placed in a graphite crucible (25 mm in diameter) and heated for 5 min in a magnetic induction furnace to 2KW (1100 °C). The glass obtained was mixed with 50 ml of  $\text{HNO}_3$  1 M solution in a polystyrene bottle. The glass bead was dissolved by the acid, then the solution obtained is filtered through a filter paper and recovering all with deionized water in a volumetric flask of 200 ml. The final solutions were analyzed by ICP-AES (inductively coupled plasma atomic emission spectroscopy) at the LMV-France, and analytical conditions were as

follows: incident power = 1050 W, reflected power < 5 W, Drainage = 0.31/min. BHVO-2 external standard was used as reference to control accuracy and deviation. The results obtained by these two different methods are consistent within analytical uncertainty (Table 7). Whole-rock trace element compositions were analyzed by inductively coupled plasma mass-spectrometry (ICP-MS) at LMV on Agilent 7500 cx. One powder sample of both aliquots (Aliquot 1: 98.4 mg and aliquot 2: 100.28 mg) was taken for trace element analysis. For dissolution, each powder sample was dissolved in a mixture solution: 1 ml 20 N of HF and 1 ml of 20 N  $\text{HNO}_3$  in a 12-ml Savillex™. The closed Savillex™ were placed on a hotplate at 100 °C for 48 h. The samples were evaporated at 70 °C. After evaporation, a second attack is carried out with a mixture of 1 ml of 30 N HCl, 4 ml of 20 N HF, and 1 ml of  $\text{HClO}_4$  and heated at 100 °C for 2 days. This step is followed by evaporation at 150 °C. A third attack with a mixture of 1 ml 30 N HCl, 4 ml 20 N and 1 ml  $\text{HClO}_4$  was carried out. The solution was then allowed to evaporate at 150 °C. The residue was dissolved in 2 ml 6 N HCl, then evaporated until all the  $\text{HClO}_4$  had been removed. The residue obtained is dissolved with recovery 10 ml 0.4 N  $\text{HNO}_3$  and diluted before analyzing.

Two blanks followed the same protocol as the sample to confirm that the NWA 4255 had not been contaminated during handling. Three mafic and ultramafic international standards (BIR1, BCR2 et JP1) were used as calibration external standards.

Fifty milligrams of powder of aliquot 1 was sent to Montpellier University to check the reliability of the data. The results obtained in the two laboratories by the solution-ICP-MS are consistent within analytical uncertainty (Table 7).

## Oxygen isotopes analyses

Oxygen isotopes analysis was undertaken on both NWA 4255 aliquots (aliquot 1 and aliquot 2, Table S1). Both aliquots were homogenized, and 2 mg of these powders was then loaded for oxygen isotope analysis at the Open University, using an infrared laser-assisted fluorination system (Miller et al. 1999; Greenwood et al. 2017). Each of the two lithologies were analyzed in duplicate. The powders were heated in the presence of  $\text{BrF}_5$ . After fluorination, the released oxygen gas was purified by passing it through two cryogenic nitrogen traps and over a bed of heated KBr. Oxygen gas was analyzed using a MAT 253 dual inlet mass spectrometer. System precision, as defined by replicate analyses ( $n = 39$ ) of our internal obsidian standard, is  $\pm 0.05\text{‰}$  for  $\delta^{17}\text{O}$ ,  $\pm 0.09\text{‰}$  for  $\delta^{18}\text{O}$ ,  $\pm 0.02\text{‰}$  for  $\Delta^{17}\text{O}$  ( $2\sigma$ ).

Oxygen isotope analyses are reported in standard  $\delta$  notation, where  $\delta^{18}\text{O}$  has been calculated as:  $\delta^{18}\text{O} = [({}^{18}\text{O}/{}^{16}\text{O})_{\text{sample}}/({}^{18}\text{O}/{}^{16}\text{O})_{\text{ref}} - 1] \times 1000$  (‰) and similarly for  $\delta^{17}\text{O}$  using the  ${}^{17}\text{O}/{}^{16}\text{O}$  ratio, the reference

being vSMOW: Vienna Standard Mean Ocean Water.  $\Delta^{17}\text{O}$ , which represents the deviation from the terrestrial fractionation line, has been calculated using the linearized format of Miller (2002):

$$\Delta^{17}\text{O} = 1000\ln(1 + \delta^{17}\text{O}/1000) - \lambda 1000\ln(1 + \delta^{18}\text{O}/1000)$$

where  $\lambda = 0.5247$ , determined using 47 terrestrial whole-rock and mineral separate samples (Miller 2002; Miller et al. 1999).

## Mineral chemistry: major and trace elements

Representative major element concentrations for orthopyroxene, chromite, and olivine are summarized in Tables 1, 2, and 3, respectively. The iron metal data compositions are given in Table 4, and the sulfide data are summarized in Table 5. The trace element concentrations for these silicates are listed in Table 6. This olivine diogenite has two distinct populations of both orthopyroxene and olivine (Figs. 4 and 5). This bimodal distribution reflects the fact that two distinct lithologies are present in NWA 4255.

## Orthopyroxenitic lithology

### Orthopyroxene

Based on the terms ferroan and magnesian used by Beck and McSween (2010), orthopyroxene in the orthopyroxenitic lithology show mainly a ferroan trend with a composition ranging from ( $\text{Wo}_1\text{En}_{73}\text{Fs}_{24}$ ) to ( $\text{Wo}_2\text{En}_{75}\text{Fs}_{26}$ ) (Table 1) and with Fe no. molar values of 24.32–26.01. These orthopyroxenes show concentrations with a slight variability for  $\text{Al}_2\text{O}_3$  (0.04–0.2 wt%),  $\text{Cr}_2\text{O}_3$  (0.2–0.4 wt%), and CaO (0.68–0.89 wt%).  $\text{TiO}_2$  concentrations are very low and often below the detection limit of the electron microprobe and never exceed 0.07 wt%. The Fe/Mn ratio of these orthopyroxenes varies from 23.91 to 32.64.

Trace element concentrations determined by LA-ICP-MS display very limited variations in orthopyroxene from orthopyroxenitic lithology. Ti ranges from 255 to 276 ppm, Co from 5.01 to 5.56 ppm, Sc from 12.1 to 13.4 ppm and V from 109 to 117 ppm. Remarkably, Ni concentrations are very low (0.254–0.386 ppm).

The high field strength element (HFSE) contents are 0.003–0.007 ppm for Hf and 0.025–0.040 ppm for Nb. Zr varies in concentrations from 0.085 to 0.217 ppm. Ta is below detection limits (less than 0.5 ppb). Moreover, incompatible trace element concentrations are very low with small variations in Y (0.094 to 0.145 ppm) and Yb (0.027–0.034 ppm).

As a consequence, in the ferroan orthopyroxenes, no correlation is observed between these elements and Ti.

The REE contents are depleted relative to CI chondrite (Anders and Grevesse 1989). Moreover, the light REE contents are generally depleted relative to heavy REE ( $\text{La}/\text{Yb}$  ranges from 0.03 to 0.08). On the other hand, middle REEs are enriched ( $\text{La}_\text{N}/\text{Sm}_\text{N} = 0.07\text{--}0.28$  and  $\text{Sm}_\text{N}/\text{Yb}_\text{N} = 0.30\text{--}0.48$ ). They show troughs at Eu in CI-normalized diagrams with a low  $\text{Eu}/\text{Eu}^*$  ranging from 0.35 to 0.66 (Fig. 6).

Although orthopyroxene from the two lithologies show REE patterns that are subparallel, the REE contents of orthopyroxene from the orthopyroxenitic lithology are more enriched, especially for the MREE and HREE ( $\text{Sm}_\text{N}/\text{Yb}_\text{N} = 0.43\text{--}0.48$ ) to those obtained on harzburgitic lithology (Fig. 6).

### Chromite

Spinel is magnesio-chromite ( $\text{Usp}_{1-2}\text{Sp}_{15-16}\text{Chr}_{81-84}$ ) with very high Cr no. values = 0.83–0.85 (Table 2). The Mg no. values of chromite show significant variation, from 15.57 to 22.45. They contain minor amounts of  $\text{TiO}_2$  (0.3–0.6 wt%). The ranges of Cr no. in this study are similar to those previously reported for NWA1877 by Irving et al. (2005) (Fig. 7).

Magnesio-chromites exhibit variable trace element concentrations: V (5369 to 5471 ppm), Ti (3462 to 3639 ppm), Co (7.81 to 10.47 ppm), Sc (5.16 to 6.39 ppm), and Ni (0.13 to 0.50 ppm). The Zr, Hf, Nb, and Ta contents range respectively from 3.83 to 3.93 ppm, 0.019 to 0.054 ppm, 3.67 to 3.93 ppm, and 0.002 to 0.008 ppm. Y ranges from 0.016 to 0.019 ppm.

## Harzburgitic lithology

### Orthopyroxene

Orthopyroxene is magnesian ( $\text{Wo}_2\text{En}_{73-76}\text{Fs}_{23-25}$ ) with Fe no. (in molar) ranging from 22.86 to 25.46. Minor element concentrations are slightly more depleted than those from orthopyroxenitic lithology  $\text{Al}_2\text{O}_3$  (0.08–0.4 wt%), CaO (0.06–0.3 wt%),  $\text{Cr}_2\text{O}_3$  (0.6–0.9 wt%),  $\text{TiO}_2$  contents are up to 0.09 wt%, but sometimes fall below detection limits.

The scarce orthopyroxene inclusions in olivine are magnesian (Mg no. 76.68 to 76.92) and show the lowest  $\text{Al}_2\text{O}_3$  (0.13 to 0.17 wt%), CaO (0.67 to 0.73 wt%) contents, the highest  $\text{Cr}_2\text{O}_3$  (0.11 to 0.18 wt%) contents among the orthopyroxene analyzed in NWA 4255.

Concentrations of Ti (207–260 ppm), V (91–124 ppm), Co (5.81–25.8 ppm), Sc (9.50–13.3 ppm), Ni (0.37–4.2 ppm), and Zr (0.029–0.103 ppm) exhibit slight variation. The contents Hf and Nb range to 0.002 to 0.004 ppm and to 0.024 to 0.036 ppm, respectively. Ta is below detection limits (less than

**Table 1** Representative microprobe analyses for orthopyroxene from NWA 4255 (in wt% oxides)

<i>n</i> <sup>o</sup>	6	28	19	27	42	3	50	8	16	57	41	58
Lithology	Harzburgitic							Orthopyroxenitic				
	Opx inclusion in olivine											
SiO <sub>2</sub>	55.51	55.57	55.70	55.83	55.64	56.21	55.90	55.57	54.93	55.13	55.47	55.06
TiO <sub>2</sub>	0.06	0.06	0.02	0.02	0.01	b.d.	0.07	0.07	0.11	0.04	0.04	0.09
Al <sub>2</sub> O <sub>3</sub>	0.17	0.33	0.27	0.31	0.31	0.13	0.16	0.35	0.33	0.40	0.29	0.36
Cr <sub>2</sub> O <sub>3</sub>	0.21	0.24	0.12	0.24	0.21	0.18	0.17	0.33	0.31	0.30	0.21	0.25
FeO	15.03	15.04	15.13	15.16	15.68	15.06	15.58	16.20	16.26	16.61	16.58	16.54
MnO	0.51	0.66	0.59	0.50	0.54	0.59	0.57	0.55	0.62	0.60	0.68	0.59
MgO	28.04	28.11	27.88	27.79	27.42	28.16	27.78	26.90	26.65	26.76	26.61	26.40
CaO	0.90	0.78	0.66	0.71	0.82	0.69	0.73	0.78	0.78	0.85	0.86	0.78
Na <sub>2</sub> O	0.11	0.01	0.02	0.00	0.04	0.03	0.02	0.02	0.00	0.00	0.04	0.03
K <sub>2</sub> O	0.00	0.02	0.00	0.02	0.02	0.00	0.01	0.01	0.01	0.00	0.00	0.00
Total	100.54	100.83	100.39	100.58	100.68	101.05	100.99	100.79	100.00	100.69	100.79	100.12
Fe/Mn	29.17	22.28	25.47	29.90	28.41	25.10	26.72	28.92	26.02	27.21	24.03	27.42
Fe/Mg	30.06	30.02	30.45	30.60	32.08	30.01	31.46	33.78	34.23	34.81	34.96	35.15
Mg #	76.89	76.91	76.66	76.57	75.71	76.92	76.07	74.75	74.50	74.18	74.10	73.99
Wo %	1.75	1.51	1.29	1.39	1.59	1.33	1.42	1.54	1.55	1.67	1.70	1.55
En %	75.54	75.75	75.67	75.50	74.51	75.89	74.99	73.60	73.34	72.94	72.84	72.84
Fs %	22.71	22.74	23.04	23.10	23.90	22.78	23.59	24.86	25.10	25.39	25.46	25.61

Mg no. =  $Mg/(Mg + Fe) \times 100$ . Fe/Mn and Fe/Mg are calculated from molar abundances

*b.d.* below detection limit

0.5 ppb). Incompatible trace element concentrations are 0.053–0.087 ppm Y and 0.017–0.022 ppm Yb.

Sc, V, and Y have a positive correlation with Ti. Sc and Ti show a clear correlation between overlapping harzburgitic and orthopyroxenitic lithologies (Fig. 5), but both show a similar trend indicating that Ti has the same behavior as Sc when

partitioning between mineral and melt. This implies that the Ti has probably a +3 valence as the Sc in this system. The REE patterns of orthopyroxene in the harzburgitic lithology are also depleted in LREE compared to HREE. La/Yb ranges from 0.05 to 0.16 and is lower than in orthopyroxenes of orthopyroxenitic lithology (Fig. 6).  $Eu/Eu^* = 0.43\text{--}0.55$ ,

**Table 2** Representative microprobe analyses for chromite of orthopyroxenitic lithology (in wt% oxides)

Fragment	50	52	44	11	19	16	3	15	4	10	20	13
SiO <sub>2</sub>	0.02	0.05	0.07	0.00	0.00	0.14	0.02	0.00	0.02	0.01	0.01	0.00
TiO <sub>2</sub>	0.37	0.46	0.56	0.57	0.63	0.52	0.51	0.62	0.54	0.64	0.49	0.35
Al <sub>2</sub> O <sub>3</sub>	7.94	7.68	7.43	7.27	7.29	6.96	7.21	7.07	7.22	7.15	7.13	7.13
Cr <sub>2</sub> O <sub>3</sub>	57.38	58.84	59.38	58.60	59.32	56.92	59.08	58.66	59.90	59.36	59.33	58.49
FeO	28.53	27.90	27.88	26.77	27.31	28.00	27.44	26.91	27.52	26.71	27.63	28.02
MnO	0.69	0.67	0.56	0.63	0.59	0.57	0.61	0.65	0.59	0.58	0.62	0.66
MgO	2.89	3.13	3.43	3.91	3.73	3.73	3.54	3.90	3.66	3.93	3.58	3.07
Total	97.82	98.74	99.30	97.75	98.87	96.85	98.41	97.86	99.44	98.41	98.79	97.72
Mg#	15.57	16.65	18.04	20.85	19.68	20.01	18.86	20.83	19.26	20.81	19.03	15.86
Cr#	82.90	83.71	84.29	84.39	84.53	84.59	84.61	84.76	84.77	84.78	84.80	84.83
Sp	15.42	16.07	15.43	15.29	15.18	14.78	15.11	14.88	14.97	14.95	14.89	14.90
Chrm	81.23	82.54	82.75	83.18	82.90	83.30	83.06	83.45	83.32	83.33	83.11	83.33
Usp	1.01	1.24	1.47	1.52	1.69	1.42	1.37	1.66	1.43	1.70	1.30	1.24

Mg no. =  $Mg/(Mg + Fe) \times 100$ . Cr no. =  $Mg/(Mg + Fe) \times 100$  calculated from molar abundances

*b.d.* below detection limit

**Table 3** Representative microprobe analyses for olivine from harzburgitic lithology (in wt% oxides)

Specific <i>n</i> <sup>o</sup>	Large grains							Small inclusions in opx				
	25	9	10	11	12	13	48	28	39	33	41	44
SiO <sub>2</sub>	38.27	38.19	38.05	38.13	37.93	37.99	38.25	38.17	36.97	37.60	38.13	37.96
TiO <sub>2</sub>	b.d.	b.d.	0.02	0.02	b.d.	b.d.	0.07	0.01	0.05	b.d.	b.d.	b.d.
Al <sub>2</sub> O <sub>3</sub>	b.d.	0.02	b.d.	b.d.	b.d.	0.02	0.02	b.d.	0.02	b.d.	0.01	b.d.
Cr <sub>2</sub> O <sub>3</sub>	0.01	b.d.	0.03	b.d.	b.d.	b.d.						
FeO	25.08	25.30	24.90	25.16	24.99	25.31	25.94	26.22	28.07	26.87	26.53	26.98
MnO	0.47	0.48	0.52	0.52	0.52	0.46	0.60	0.67	0.61	0.59	0.60	0.60
MgO	36.80	36.68	36.91	37.06	37.08	37.00	36.21	35.60	34.68	35.50	35.26	35.36
CaO	0.06	0.01	0.03	0.04	0.02	0.02	0.01	0.06	0.07	b.d.	0.02	0.05
Na <sub>2</sub> O	0.02	0.03	b.d.	0.03	b.d.	b.d.	b.d.	b.d.	b.d.	b.d.	b.d.	b.d.
Total	100.70	100.74	100.47	100.98	100.58	100.80	101.09	100.73	100.50	100.56	100.56	100.95
Fe/Mn	52.73	51.37	47.02	47.71	47.03	54.04	42.42	38.77	45.17	45.12	43.29	44.17
Mg#	72.34	72.10	72.55	72.42	72.57	72.27	71.33	70.76	68.77	70.19	70.32	70.02
Fa	27.66	27.90	27.45	27.58	27.43	27.73	28.67	29.24	31.23	29.81	29.68	29.98

Mg no. =  $Mg/(Mg + Fe) \times 100$ . Fe/Mn and Fe/Mg are calculated from molar abundances

*b.d.* below detection limit

Sm<sub>N</sub>/Yb<sub>N</sub> ranges from 0.26 to 0.36 and La<sub>N</sub>/Sm<sub>N</sub> ratio from 0.18 to 0.64.

## Olivine

Olivine also displays a bimodal distribution, Fe no. ranges from 27.43 to 29.06 for large grains and to 28.39 to 32.01 for small grains (Fig. 4). These values agree well with the compositions from olivine-bearing diogenites (Shearer et al. 2010). The Fe/Mn ratio displays wide variation from 38.8 to 72.7. The abundance of minor elements is very low and below detection limit of the electron microprobe.

On the basis of LA-ICP-MS measurements of olivine from harzburgitic lithology, Ti ranges from 38.04 to 48.70 ppm, and Ca contents range from 315 to 1215 ppm. Ni and Co contents of olivine show a wide variation Ni (2.94 to 23.15 ppm) vs. Co (17.8 to 133 ppm). Ni exhibits a positive correlation with Co as shown in (Fig. 8), with a mean Ni/Co ratio of 0.26. V contents in these olivines yield concentrations ranging from 14 to 16.1 ppm and Sc in the range 3.73 to 4.1 ppm. In addition, Zr content is 0.019 ppm, and Nb concentrations range from 0.002 to 0.007 ppm. Hf and Ta contents are below detection limits. Y contents vary from 0.003 to 0.016 ppm and Yb contents from 0.002 to 0.007 ppm.

**Table 4** Representative microprobe analyses of Iron metal from orthopyroxenitic and harzburgitic lithologies (wt% element)

Lithology <i>n</i> <sup>o</sup>	Orthopyroxenitic					Harzburgitic						
	3	12	23	25	15	7	19	16	17	20	19	30
Si	0.06	0.02	0.01	0.01	b.d.	0.02	b.d.	b.d.	0.01	b.d.	b.d.	b.d.
S	0.03	0.02	0.01	0.04	b.d.	0.01	b.d.	0.01	0.01	b.d.	b.d.	0.01
Fe	98.16	98.68	99.04	99.36	99.41	99.59	99.74	99.75	99.75	99.83	99.83	99.83
Co	0.45	0.46	0.51	0.49	0.28	0.30	0.41	0.34	0.34	0.38	0.39	0.42
Ni	0.14	0.12	b.d.	0.13	0.10	b.d.	0.09	b.d.	b.d.	b.d.	0.11	b.d.
Mg	b.d.	b.d.	b.d.	0.01	0.01	b.d.	b.d.	0.01	0.01	0.01	b.d.	b.d.
Mn	0.05	0.04	0.03	0.01	b.d.	0.01	b.d.	0.01	b.d.	0.02	0.01	b.d.
Cr	0.09	0.05	0.07	0.02	b.d.	0.02	b.d.	0.01	0.11	0.59	0.02	b.d.
Total	98.98	99.39	99.76	100.05	99.80	99.99	100.24	100.15	100.27	100.86	100.36	100.32
Fe/Ni	717.02	836.96		786.07	982.32		1102.14				930.38	
Ni/Co	0.30	0.26		0.26	0.36		0.22				0.27	

**Table 5** Representative microprobe analyses for sulfides from harzburgitic and orthopyroxenitic lithology (wt% element)

n°	Harzburgitic lithology								Orthopyroxenitic lithology			
	28	21	36	38	11	51	17	45	13	3	41	39
S	36.66	35.73	36.77	36.86	36.78	36.54	37.08	36.81	36.62	36.31	36.58	35.30
Si	0.02	0.08	0.01	0.04	0.01	0.04	0.05	0.02	b.d.	0.01	b.d.	0.04
Fe	62.99	62.36	62.83	62.53	62.74	62.82	62.22	62.17	61.60	62.29	61.78	61.88
Co	b.d.	0.04	b.d.	b.d.	b.d.	b.d.	b.d.	b.d.	b.d.	b.d.	b.d.	b.d.
Ni	0.01	0.01	b.d.	b.d.	b.d.	b.d.	b.d.	0.02	0.02	b.d.	b.d.	0.01
Mg	b.d.	0.01	0.02	0.01	b.d.	0.01	b.d.	b.d.	b.d.	0.01	b.d.	b.d.
Mn	b.d.	0.06	0.04	0.01	0.02	b.d.	0.03	0.01	0.04	b.d.	b.d.	0.03
Cr	0.01	0.03	0.08	0.02	0.04	0.07	0.11	1.57	2.29	2.34	2.42	2.82
Cu	b.d.	b.d.	b.d.	0.05	0.07	b.d.	b.d.	0.04	0.05	0.03	0.01	0.02
Sum	99.69	98.32	99.75	99.51	99.65	99.48	99.50	100.64	100.62	100.99	100.79	100.10
Fe/Ni	4531	5376	–	–	–	–	–	3342	3802	–	–	10668

## In all lithologies from NWA 4255

### Iron metal and sulfides

In both lithologies from NWA 4255, iron metal displays a very low Ni content ( $\text{Ni} < 0.1 \text{ wt}\%$ ) and Co content ranges from 0.27 to 0.59 wt.% (Table 4). The mean Ni/Co ratio is similar to the olivine ratio (0.26) and extends the observed correlation.

Sulfides are troilite (FeS) with a very low content of transition metals, generally below the detection limit of the electron microprobe (Table 5). Furthermore, Troilite inclusions in chromite are Cr-rich (1.57–3.43 wt%).

$\text{Cr}_2\text{O}_3$  and CaO increase with  $\text{Al}_2\text{O}_3$  in the orthopyroxene of both lithologies and show a broad correlation from harzburgitic orthopyroxene to orthopyroxenitic orthopyroxenes, with an overlap between them. On the other hand, major and minor element abundances show a narrow overlap between magnesian and ferroan orthopyroxene. The Fe/Mn ratio in orthopyroxene of both lithologies shows a wide overlap (Fe/Mn 22.28–30.94 and 23.91–32.64 for magnesian orthopyroxenes and ferroan orthopyroxenes respectively). Whatever, the lithology Sc, Y, and V correlates with Ti. These variation trends are more evident in harzburgitic lithology and differ from those in the literature (Fowler et al. 1995; Shearer et al. 2010). Compared with diagenitic orthopyroxenes discussed in the literature, orthopyroxenes in NWA 4255 display very low trace element contents and are among the poorest in compatible and trace elements. This evidence supports the possibility that these orthopyroxenes crystallized from a very primitive melt.

Orthopyroxenes from harzburgitic lithology and containing olivine inclusions display intermediate compositions between orthopyroxene include in olivine and orthopyroxene from orthopyroxenitic lithology. This reinforces the idea that there is a co-genetic link between the both lithologies.

## Whole-rock geochemistry

The whole-rock data for NWA 4255 are listed in Table 7. Chondrite CI-normalized rare earth elements patterns show that NWA 4255 has a flat shape for light and intermediate rare earth elements. The La varies from 125 ppb CI to 258 ppb CI, and the  $\text{Yb}_N$  varies from 203 ppb CI to 231 ppb CI. They are highly depleted in comparison with CIs, especially for LREEs and MREEs ( $(\text{La}/\text{Sm})_N = 0.19\text{--}0.64$ ). They show Eu troughs with a low average  $\text{Eu}/\text{Eu}^*$  ( $\text{Eu}_N/(\text{Sm}_N \cdot \text{Gd}_N)^{1/2}$ ) ratio of 0.47. The  $\text{Ce}/\text{Ce}^*$  ( $\text{Ce}_N/(\text{La}_N \cdot \text{Pr}_N)^{1/2}$ ) ratios range from 0.97 to 1.02. The NWA 4255 has Fe no. ( $\text{Fe}/(\text{Fe} + \text{Mg})$ ) of 25.88. The average Fe/Mn ratio is 28.93. Average concentrations for Sc and Ti are 12 and 263 ppm, respectively. It should be noted that the data shows troughs at Th and Pb and peaks at Ba, U, and Ti (Fig. 9).

## Oxygen isotope analysis

Duplicate analyses of both of the two main lithologies in NWA 4255 gave essentially identical results within error, with the harzburgite having the composition:  $\delta^{17}\text{O} = 1.675 \pm 0.007\text{‰}$  ( $2\sigma$ ),  $\delta^{18}\text{O} = 3.642 \pm 0.016\text{‰}$  ( $2\sigma$ ),  $\Delta^{17}\text{O} = -0.234 \pm 0.001\text{‰}$  ( $2\sigma$ ) and the orthopyroxenite:  $\delta^{17}\text{O} = 1.682 \pm 0.016\text{‰}$  ( $2\sigma$ ),  $\delta^{18}\text{O} = 3.656 \pm 0.010\text{‰}$  ( $2\sigma$ ),  $\Delta^{17}\text{O} = -0.234 \pm 0.010\text{‰}$  ( $2\sigma$ ) (Table S1). Both lithologies have  $\Delta^{17}\text{O}$  values that are close to the mean  $\Delta^{17}\text{O}$  value of  $-0.241 \pm 0.018 \text{‰}$  ( $2\sigma$ ) obtained by Greenwood et al. (2017) for 105 eucrite and diagenite analyses, both falls and finds. This indicates that the harzburgite and orthopyroxenite lithologies in NWA 4255 are both normal members of the HED suite.

**Table 6** Trace element concentrations (ppm) for orthopyroxene, olivine, and chromite in NWA 4255

Lithology	Harzburgitic										
	Orthopyroxene					Olivine					
<i>n</i> °	9	10	16	3	4	5	6	7	8	14	15
Ca	4972	4792	4216	–	–	1215	429	315	338	–	–
Sc	13.3	11.7	9.5	6.61	7.21	4.1	3.77	4.01	3.73	3.8	3.40
Ti	260	239	207	–	–	48.7	38	43	39.4	40.56	32.58
V	124	108	91	60.93	64.65	16.1	15.4	14	16.1	16.76	16.16
Cr	2254	1776	1331	704.27	750.63	57	58	45	53	59.05	50.31
Co	13.2	5.81	25.8	537.44	81.75	133	51	19.9	17.9	158.52	25.50
Ni	4.2	0.371	3.07	99.7	15.04	23.15	10.6	3.73	2.94	26.62	5.05
Rb	0.006	0.004	0.008	–	–	0.016	0.004	0.014	0.067	–	–
Sr	0.19	0.320	1.32	–	–	11.04	2.1	2.09	4.57	–	–
Y	0.087	0.078	0.053	0.05	0.04	0.009	0.003	0.004	0.016	–	–
Zr	0.103	0.053	0.029	0.04	0.06	0.019	b.d.	b.d.	b.d.	–	–
Nb	0.036	0.025	0.024	0.03	0.02	0.007	0.002	0.002	0.005	–	–
Ba	b.d.	b.d.	b.d.	13.06	2.81	6.321	0.949	1.604	4.698	–	–
La	0.005	0.002	0.002	0.01	0.01	0.003	0.001	0.003	0.014	–	–
Ce	0.013	0.005	0.009	–	–	0.004	0.002	0.008	0.036	–	–
Pr	0.002	0.001	0.002	–	–	0.001	b.d.	0.001	0.004	–	–
Nd	0.013	0.010	0.010	–	–	0.007	b.d.	0.004	0.016	–	–
Sm	0.005	0.005	0.006	–	–	b.d.	b.d.	b.d.	0.005	–	–
Eu	0.001	0.001	b.d.	–	–	b.d.	b.d.	b.d.	b.d.	–	–
Gd	0.009	0.008	0.006	–	–	b.d.	b.d.	b.d.	b.d.	–	–
Tb	0.002	0.001	0.001	–	–	b.d.	b.d.	b.d.	0.001	–	–
Dy	0.013	0.011	0.008	–	–	b.d.	b.d.	0.002	0.004	–	–
Ho	0.003	0.003	0.002	–	–	0.001	b.d.	b.d.	b.d.	–	–
Er	0.010	0.012	0.008	–	–	b.d.	b.d.	b.d.	0.003	–	–
Tm	0.003	0.003	0.002	–	–	0.001	b.d.	b.d.	0.001	–	–
Yb	0.021	0.022	0.017	–	–	0.002	b.d.	b.d.	0.007	–	–
Lu	0.005	0.005	0.004	–	–	0.001	0.001	0.001	0.001	–	–
Hf	0.003	0.004	0.002	–	–	0.001	b.d.	b.d.	0.002	–	–
Ta	b.d.	b.d.	b.d.	–	–	b.d.	b.d.	b.d.	b.d.	–	–
Pb	0.004	0.002	0.005	–	–	0.021	0.006	0.010	0.036	–	–
Th	0.001	b.d.	b.d.	–	–	0.001	b.d.	0.001	0.002	–	–
U	b.d.	b.d.	b.d.	–	–	0.029	0.011	0.004	0.017	–	–
Ni/Co	0.318	0.064	0.119	0.19	0.18	0.174	0.209	0.187	0.165	0.17	0.20
(La/Yb) <i>n</i>	0.16	0.05	0.10	–	–	0.92	–	–	1.30	–	–
(La/Sm) <i>n</i>	0.64	0.19	0.27	–	–	–	–	–	1.85	–	–
(Sm/Yb) <i>n</i>	0.25	0.26	0.36	–	–	–	–	–	0.70	–	–
Eu/Eu*	0.43	0.55	–	–	–	–	–	–	–	–	–
Ce/Ce*	3.71	3.76	4.84	–	–	3.05	–	5.16	5.10	–	–
Lithology	Orthopyroxenitic										
	Orthopyroxene					Chromite					
<i>n</i> °	20	17	18	1	2	11	12	13	19		
Ca	–	4969	4855	5031	4908	72	54	30	84		
Sc	13.41	13.4	12.6	12.5	12.1	6.39	6.08	5.71	5.16		
Ti	–	276	259	264	255	3516	3460	3640	3544		
V	112.74	113	109	117	117	5469	5471	5457	5369		
Cr	1666.43	1666	1664	2122	2076	376242	376242	376242	376242		
Co	5.01	5.01	5.14	5.50	5.56	10.5	11.7	7.8	9.8		

**Table 6** (continued)

Ni	0.39	0.386	0.309	0.238	0.254	0.133	0.291	0.389	0.50
Rb	–	0.008	0.011	b.d.	b.d.	0.006	0.005	0.004	0.012
Sr	–	0.209	0.190	0.217	0.182	0.199	0.211	0.246	0.263
Y	–	0.098	0.094	0.145	0.137	0.016	0.018	0.018	0.019
Zr	–	0.085	0.114	0.217	0.201	3.83	3.9	3.91	3.93
Nb	–	0.025	0.026	0.040	0.029	3.73	3.75	3.67	3.93
Ba	–	0.067	0.077	b.d.	0.014	b.d.	0.016	0.066	0.126
La	–	0.002	0.003	0.002	0.002	b.d.	b.d.	b.d.	0.008
Ce	–	0.008	0.013	0.012	0.009	0.003	0.002	b.d.	0.008
Pr	–	0.002	0.002	0.003	0.003	b.d.	b.d.	b.d.	0.001
Nd	–	0.018	0.017	0.028	0.024	b.d.	b.d.	b.d.	0.013
Sm	–	0.007	0.008	0.015	0.012	0.003	b.d.	b.d.	b.d.
Eu	–	0.002	0.002	0.002	0.002	b.d.	b.d.	b.d.	b.d.
Gd	–	0.010	0.011	0.018	0.016	b.d.	b.d.	b.d.	b.d.
Tb	–	0.002	0.002	0.002	0.003	0.001	b.d.	b.d.	b.d.
Dy	–	0.014	0.015	0.022	0.024	b.d.	b.d.	b.d.	b.d.
Ho	–	0.003	0.003	0.005	0.005	b.d.	b.d.	b.d.	b.d.
Er	–	0.015	0.014	0.020	0.021	b.d.	b.d.	b.d.	b.d.
Tm	–	0.002	0.003	0.003	0.004	b.d.	b.d.	b.d.	b.d.
Yb	–	0.027	0.029	0.034	0.032	b.d.	b.d.	b.d.	b.d.
Lu	–	0.005	0.005	0.005	0.005	b.d.	b.d.	b.d.	b.d.
Hf	–	0.003	0.003	0.007	0.007	0.023	0.023	0.054	0.019
Ta	–	b.d.	b.d.	b.d.	0.001	0.008	0.009	0.002	0.008
Pb	–	0.006	0.010	0.005	0.005	b.d.	0.003	0.006	b.d.
Th	–	b.d.	0.001	b.d.	b.d.	b.d.	b.d.	b.d.	b.d.
U	–	b.d.							
Ni/Co	0.077	0.077	0.060	0.043	0.046	0.013	0.025	0.050	0.05
(La/Yb) <sub>n</sub>	–	0.05	0.08	0.03	0.04	–	–	–	–
(La/Sm) <sub>n</sub>	–	0.18	0.28	0.07	0.09	–	–	–	–
(Sm/Yb) <sub>n</sub>	–	0.30	0.30	0.48	0.43	–	–	–	–
Eu/Eu*	–	0.66	0.56	0.42	0.35	–	–	–	–
Ce/Ce*	–	3.41	4.59	5.14	4.13	–	–	–	2.76

Values normalized to CI chondrite (Anders and Grevesse 1989).  $Eu/Eu^* = Eu_n / ((Sm_n \times Gd_n)^{1/2})$ .  $Ce/Ce^* = Ce_n / ((La_n \times Pr_n)^{1/2})$

*b.d.* below detection limit

## Discussion

### Phase equilibria

On the diagram of Fe no. Opx versus Fe no. Olivine (Fig. 10), couples of compositions of olivines and orthopyroxenes with textural equilibrium (original magmatic boundaries) are represented. These data fall almost exactly on the equilibrium line, defined by Mittlefehldt (1994). Olivines and orthopyroxenes from Harzburgitic lithology are in chemical equilibrium. We distinguish a progressive chemical evolution in the NWA 4255, with an iron enrichment when the olivine grains become smaller and smaller and scarcer and scarcer. This reflects both the progressive differentiation of the magma and the advancement of the peritectic reaction consuming the olivine. This suggests that during magmatic evolution and peritectic reaction, the phase's compositions remained in equilibrium. This observation is in contradiction with the results of Beck and McSween (2010) whose brecciated samples show erratic Fe no. Opx versus Fe no. Olivine compositions. They interpret this as evidence of an intimate mixture of no co-genetic harzburgitic and diogenitic rocks by intense

brecciation linked to meteorite impacts. These evidences provide support for a genetic relationship between the various lithologies of NWA 4255.

Olivine, orthopyroxene, and iron metal of the harzburgitic and orthopyroxenitic lithologies, as well as the whole-rock analysis, are aligned on the same evolution trend (Fig. 11). This shows that the whole rock is the mixture of these different phases. On the other hand, the fact that the Ni/Co ratio is relatively constant supports the hypothesis of a co-genesis of the different phases (Figs. 8 and 12). This low Ni/Co ratio seems linked to the very low abundance of Ni in the melt at the origin of NWA4255. Moreover, some orthopyroxenes in orthopyroxenitic lithology are slightly shifted to even lower values of Ni and deviate from this trend. The abundance of sulfide inclusions in these orthopyroxenes may represent a sink for this siderophile and chalcophilic element at the expense of orthopyroxene. The Cr/V ratio in the orthopyroxene varies between 0.24 and 0.38. This ratio, based on the work of Cartier et al. (2014), implies that the  $fO_2$  was well below Iron-Wustite buffer (IW-7). This is lower than the estimates for diogenites and eucrites (IW-2) of Boesenberg and Delaney (1997). Under these conditions, the iron metal could have

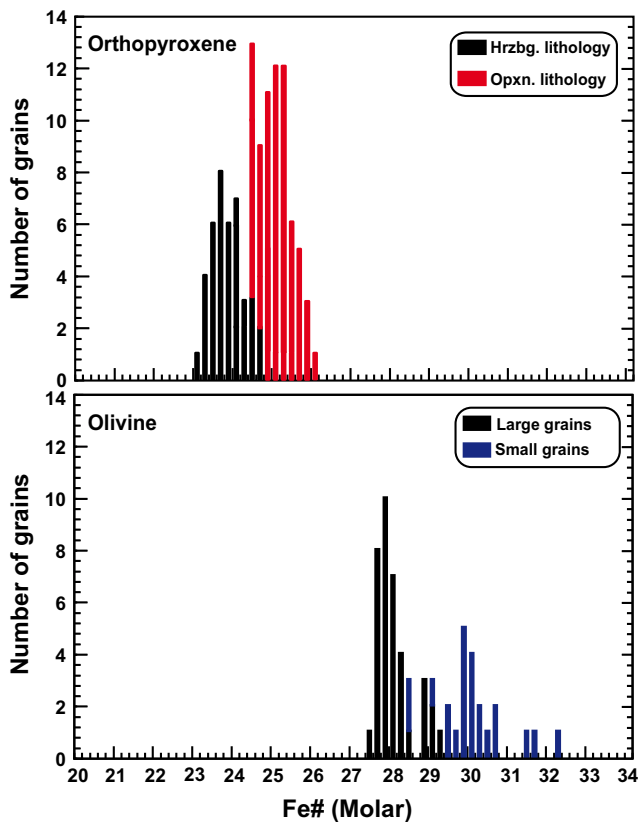


**Fig. 4** Frequency histograms for orthopyroxene and olivine Fe no. [ $100 \times \text{Fe}/(\text{Fe} + \text{Mg})$  in molar] in NWA 4255. Upper diagram: Two distinct populations of orthopyroxene are present. Magnesian composition (harzburgitic Opx) ranges from 22.86 to 25.46 and the ferroan composition (orthopyroxenitic Opx) ranges from 24.4 to 26.01. Lower diagram: olivine shows two distinct populations, with a narrow composition for the large crystals and a slightly larger variation for the small crystals

been present as a liquidus phase. This metal appears after the formation of the metal core that has probably a chondritic Ni/Fe ratio, and it originates from the differentiation of magma

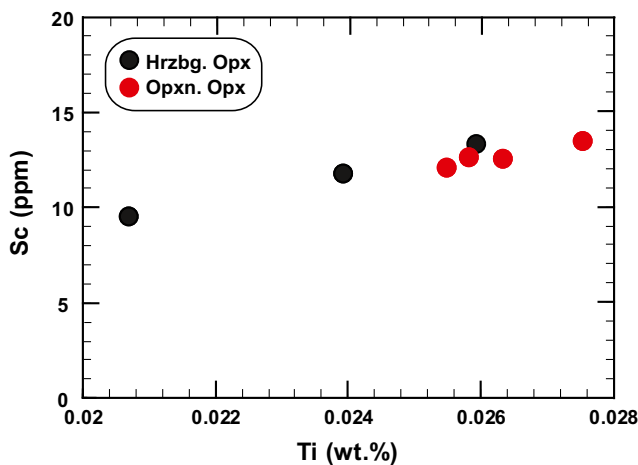


**Fig. 5** Positive correlation between the Sc and Ti in the harzburgitic orthopyroxenes, whereas orthopyroxene in the orthopyroxenitic lithology shows more restricted Ti variation

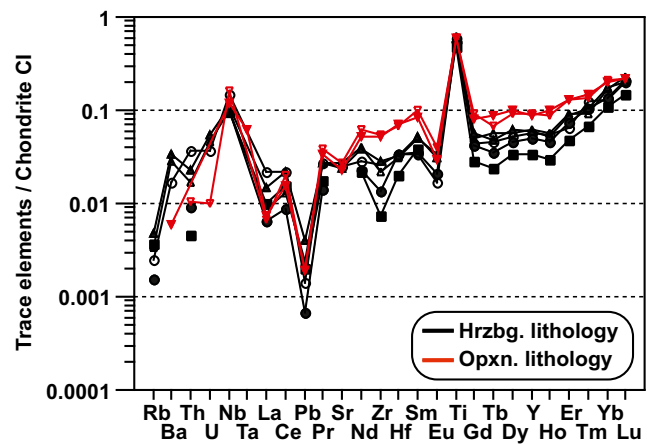


**Fig. 6** Trace elements patterns for orthopyroxene from orthopyroxenitic and harzburgitic lithologies of NWA 4255, normalized to Chondrites CI (Anders and Grevesse 1989)

and the rapid attainment of iron saturation at very low oxygen fugacity. This implies that the metal in NWA 4255 is not related to a metal-rich precursor, and so was not chondritic metal brought in by impactors, but a metal precipitate formed under liquidus conditions and in chemical equilibrium with the silicate melt, as well as with both olivine and orthopyroxene.

**Petrogenetic relationship between the two main lithologies present in NWA 4255**

Firstly, the harzburgitic lithology consists of orthopyroxene, olivine, and iron metal. Olivine shows an increase in Fe no. as its crystal size decreases. This most likely reflects a peritectic reaction between olivine and melt to produce orthopyroxene.

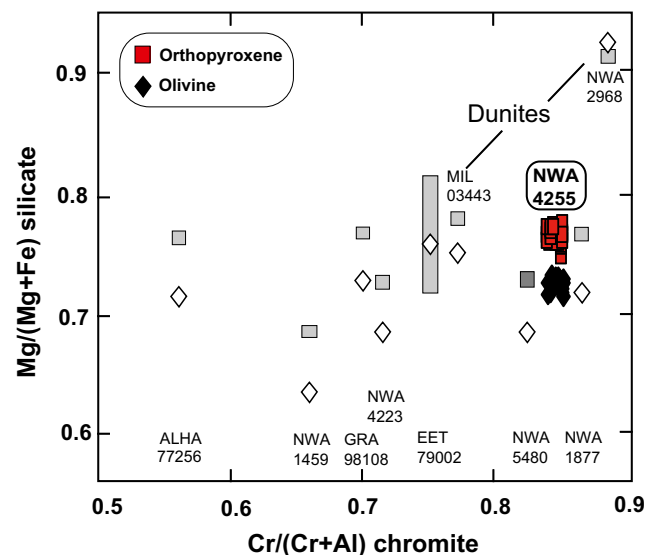


**Fig. 7** Mg no. for silicates vs Cr no. for chromite shows a comparison between this study and other olivine diogenites (Irving et al. 2009)

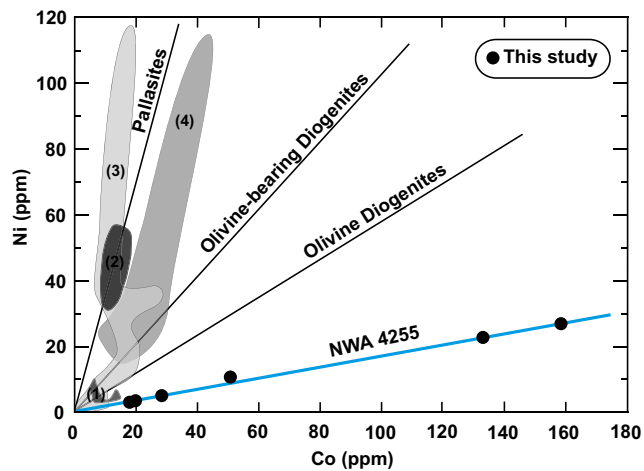


**Fig. 8** Ni versus Co diagram for olivine from NWA 4255. Compositions for NWA 4255 fall on a linear trend distinct from any previously discussed in the literature. The literature data used in this diagram are from: (1) Lunning et al. (2015); (2) (Shearer et al. 2010); (3) and (4) (Hahn et al. 2018)

In addition, the orthopyroxenitic lithology consists of orthopyroxene and spinel but is devoid of olivine. It is also more enriched in Fe no. than the harzburgitic lithology and display higher incompatible trace element contents. This implies that the olivines reacting with the liquid along the peritectic produce orthopyroxene, which shields the olivine and isolates it from the residual melt. The liquid then evolves out of the peritectic and produces orthopyroxene and spinel by fractional crystallization.

### Evolution of minor and trace elements

The concentration of trace elements in NWA 4255 are slightly varied between the different aliquots as is the case in other diogenites and olivine diogenites (Barrat et al. 2006; Fowler et al. 1994, 1995; Mittlefehldt 1994, 2015; Shearer et al. 1997, 2010). These concentrations are low compared with those known in the literature, implying that it is among the most primitive or the less evolved diogenites. Despite this low content, we still observed positive correlations between the Sc, V, and Y with Ti. This could be explained by a similar behavior during orthopyroxene crystallization linked to a change in the valence of titanium to 3+. This implies that most of the Ti is present in the 3+ valence that it is coherent with the very low calculated oxygen fugacity (IW-7). Note that these correlations are only observed in the harzburgitic orthopyroxene, but not in the orthopyroxene of the orthopyroxenitic lithology. This could imply that the harzburgitic lithology is more reduced than the orthopyroxenitic lithology which is also supported by the presence of metal.

In addition, the concentration of Yb and the REEs increase from the harzburgitic to orthopyroxenitic lithology. This suggests that this is linked to the decrease of melt mass, and that

orthopyroxene in the orthopyroxenitic lithology crystallized after the crystallization of harzburgitic orthopyroxene, as proposed by Beck et al. (2013). Additionally, the REE patterns displayed by the orthopyroxenitic orthopyroxenes have characteristic shapes (MREE enrichment) that are different from those of the harzburgitic orthopyroxenes. The difference in shape of REE pattern indicates that the orthopyroxenes of orthopyroxenitic lithology are the strict product of mineral-melt equilibrium between chondritic melt and orthopyroxene, as confirmed by the Onuma diagram (Fig. S1). The REE pattern of orthopyroxene in harzburgitic lithology indicates a more complex mechanism involving a distribution of REE between olivine-orthopyroxene-melt and reflecting the peritectic reaction. The REE patterns show a progressive enrichment of middle and heavy rare earth elements from the harzburgitic orthopyroxene to the orthopyroxenitic orthopyroxene. This confirms the progress of the peritectic reaction between the minerals formed and the liquid involving more and more orthopyroxene and less and less olivine. When the liquid leaves the peritectic, it passes into the field of orthopyroxene + liquid resulting in the formation of orthopyroxene only (Fig. 12).

### Petrogenesis of olivine diogenite and diogenite

Large grains of olivine are only observed in the harzburgitic lithology; they are more magnesian than the small grains. This implies that the most magnesian olivine crystals are consumed by the peritectic reaction and transformed into orthopyroxene (Fig. 12).

Olivine and spinel show preservation of magmatic boundaries with orthopyroxene indicating that the primary relationship between the various lithologies in NWA 4255 was controlled by igneous events. In contrast, the brecciation that is commonly present in the sample represents a secondary process, which obviously occurred after the crystallization of the mineral phases.

We propose that the two lithologies in this olivine diogenite (NWA 4255) are genetically linked; furthermore, they represent a continuation of a magmatic crystallization sequence that evolved from the harzburgitic to the orthopyroxenitic lithology. Additionally, this provides the most cogent evidence confirming that the association between the lithologies is not the result of brecciation, but instead represents a magmatic evolution in the olivine diogenite. The scheme presented here for NWA 4255 is in contrast to that proposed by Beck and McSween (2010) for their samples. These authors suggest that magnesian orthopyroxenes, ferroan orthopyroxenes, and olivine in close proximity were not in chemical equilibrium, but instead represent the product of brecciation of a harzburgitic lithology and an orthopyroxenitic lithology that were then subsequently mixed to produce their samples (Fig. 10).

**Table 7** Major and trace element compositions of whole rock from NWA 4255

	Aliquot 1 Glass bids (Nancy) (1560 mg)	Aliquot 1 ICP-AES (LMV) (1560 mg)	Aliquot 2 ICP-AES (LMV) (1570 mg)	Average	Standard deviation
Mass (mg)	5	100	100		
SiO <sub>2</sub> (wt%)	53.16	53.46	54.03	53.55	0.44
TiO <sub>2</sub>	0.07	0.08	0.05	0.07	0.01
Al <sub>2</sub> O <sub>3</sub>	0.49	0.64	0.62	0.58	0.08
Cr <sub>2</sub> O <sub>3</sub>	0.56			0.56	
FeO	16.29	16.93	16.79	16.67	0.34
MnO	0.55	0.58	0.57	0.57	0.01
MgO	26.51	27.27	26.60	26.79	0.41
CaO	0.84	0.81	0.78	0.81	0.03
Na <sub>2</sub> O	0.07	0.15	0.12	0.11	0.04
K <sub>2</sub> O	0.05	0.17	0.12	0.12	0.06
NiO	0.02	–	–	0.02	
Sum	98.61	100.11	99.73		
	(Mntp.)	ICP-MS (LMV)	ICP-MS (LMV)		
Mass (mg)	50	98.4	100.28		
Li (ppm)	1.2	1.23	1.22	1.22	0.02
Sc	13.2	11.5	11.9	12.2	0.90
Ti	278	260	252	263	13.3
V		169	147	158	15.6
Cr		5455	3948	4701	1065
Mn		3862	3962	3912	70.7
Co	14.7	15.5	13.4	14.5	1.06
Ni	3.7	2.43	2.17	2.77	0.82
Cu	3.1	2.9	2.42	2.82	0.35
Rb	0.079	0.077	0.139	0.098	0.04
Sr	1.368	1.12	1.46	1.32	0.18
Y	0.167	0.168	0.184	0.173	0.01
Zr	0.443	0.417	0.619	0.493	0.11
Nb	0.036	0.028	0.037	0.034	0.01
Cs	0.005			0.005	
Ba	2.25	2.22	1.40	1.957	0.48
La	0.032	0.029	0.061	0.041	0.02
Ce	0.078	0.069	0.140	0.096	0.04
Pr	0.011	0.010	0.018	0.013	0.00
Nd	0.054	0.051	0.076	0.060	0.01
Sm	0.018	0.018	0.024	0.020	0.00
Eu	0.003	0.003	0.004	0.004	0.00
Gd	0.024	0.020	0.025	0.023	0.00
Tb	0.004	0.004	0.005	0.004	0.00
Dy	0.031	0.026	0.029	0.029	0.00
Ho	0.007	0.006	0.007	0.007	0.00
Er	0.025	0.019	0.022	0.022	0.00
Tm	0.004	0.004	0.005	0.004	0.00
Yb	0.037	0.038	0.033	0.036	0.00
Lu	0.008	0.006	0.007	0.007	0.00
Hf	0.014	0.013	0.020	0.016	0.00
Ta	0.002	0.002	0.002	0.002	0.00
Pb	0.067	0.066	0.134	0.089	0.04

**Table 7** (continued)

	Aliquot 1 Glass bids (Nancy) (1560 mg)	Aliquot 1 ICP-AES (LMV) (1560 mg)	Aliquot 2 ICP-AES (LMV) (1570 mg)	Average	Standard deviation
Th	0.008	0.007	0.017	0.011	0.01
U	0.007	0.006	0.008	0.007	0.00
(La/Sm) <i>n</i>	1.14	1.00	1.57	1.24	0.30
(Gd/Lu) <i>n</i>	0.431	0.461	0.534	0.475	0.05
Eu/Eu*	0.429	0.507	0.462	0.466	0.04
Ce/Ce*	1.01	0.97	1.02	1.00	0.03

The reference of normalization is the CI chondrite (Anders and Grevesse 1989).  $Eu/Eu^* = (Eu_N / (Sm_N * Gd_N))^{1/2}$ .  $Ce/Ce^* = (Ce_N / (La_N * Pr_N))^{1/2}$

The high ratio of Cr no. in the chromite of NWA 4255 (as NWA 1877 Diogenite) (Fig. 7) is previously interpreted as residual spinel from the mantle (Irving et al. 2005), precipitate from a primitive melt at chromium saturation according to Irvine (1977) and the chemical estimations of the silicate fraction of 4Vesta (Lodders 2000).

**The Fe/Mn ratio**

Fe/Mn ratio in orthopyroxenes of both lithologies varies from 22.28 to 32.64; in addition, it shows a large overlap between them. This ratio is different from what is known for diogenites (Beck and McSween 2010) but is similar to that seen in some olivine diogenites (Beck and McSween 2008) and other HED samples (Mayne et al. 2009). This leads us to raise the question about the Fe/Mn ratio and why it is so different despite the fact that NWA 4255 shows most of the diagnostic characteristics of a diogenite from 4Vesta. A different orthopyroxene Fe/Mn in olivine diogenites than in regular diogenite would suggest complex crystallization processes on 4Vesta (Beck and McSween 2008). Furthermore, the Ni/Co in olivine is also different in NWA 4255 compared to other diogenites (Fig. 8).

**Oxygen isotopes**

As discussed above, both the harzburgitic and orthopyroxenitic lithologies in NWA 4255 have closely similar oxygen isotope compositions. This supports the conclusions based on petrography and major and trace element geochemistry, indicating that the two major lithologies in NWA 4255 are genetically related to each other.

**MELTS modeling**

In this section, we use the model of Mandler and Elkins-Tanton (2013) to discuss the likely formation mechanism of the lithological variation observed in NWA 4255. We look at the differentiation and crystallization of the Vestian magmatic ocean, to see how NWA 4255 might be placed in the overall crystallization sequence. In particular, we focus on the formation of olivine diogenites and diogenites in general.

We chose as our starting material the composition suggested by Boesenberg and Delaney (1997) for the bulk silicate composition of 4Vesta. However, our conclusions would be equally valid if we had chosen a different composition, such as those suggested by Dreibus and Wänke (1980), Lodders (2000); Ruzicka et al. (1997), as compiled by Mandler and Elkins-Tanton (2013). Since, all of these compositions are very similar to each other. We used as the starting conditions for our modeling: IW-7, T = 1622 °C, P = 100 bar (< 1 kb because this is the maximum pressure in the center of 4Vesta if we consider its diameter (530 km) and its average gravity (0.22 m/s<sup>2</sup>). Using the pMELTS software (Ghiorso et al. 2002), we calculated the compositions of the resulting solids and the modal proportion of each mineral phase. We controlled the liquid in each step and also the evolution of the liquid.

We took the composition of the vestian magmatic ocean (Fig. 13, Liquid 1) which undergoes a crystallization rate of 70%. The 70% solids formed (Fig. 13, solid 1) represent a harzburgitic mantle comprising 63% olivine (Fo79), 36% orthopyroxene (Wo2En81Fs17), and 1% spinel (Mg no. 51.48 and Cr no. 72.86). (Fig. 13). The solid mantle formed

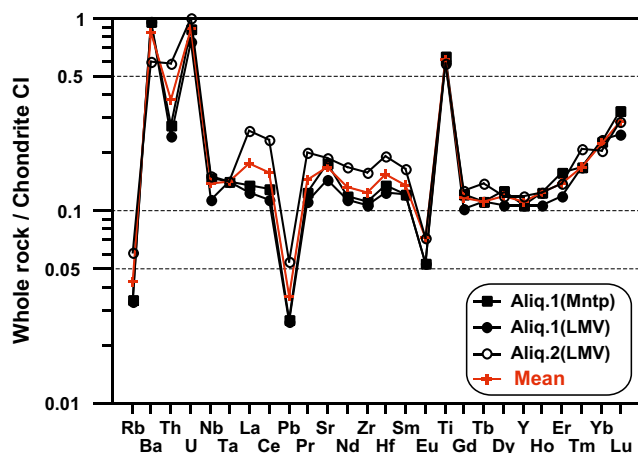
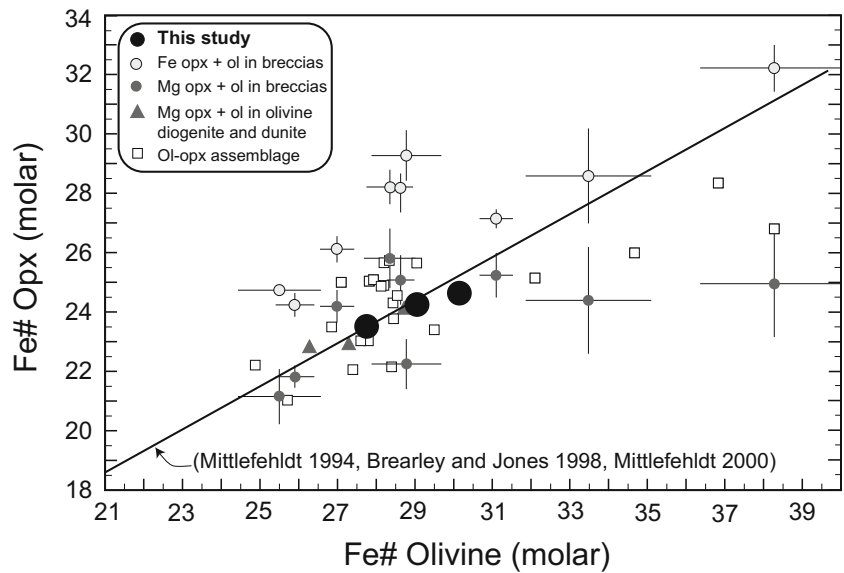


**Fig. 9** Whole-rock trace elements (a) and REE (b) patterns normalized to Chondrites CI (Anders and Grevesse 1989) for the NWA 4255 olivine diogenite. The abbreviations are defined in Table 7

**Fig. 10** Fe no. for orthopyroxene vs. Fe no. for olivine from harzburgitic lithology of NWA 4255. The literature data used in this diagram are from (Beck and McSween 2010). The data of this study falls almost exactly on the equilibrium line



was separated, and the remaining 30% liquid was restarted and cooled under the same equilibrium conditions. We are able to reproduce the modal and chemical compositions of NWA4255 with 22% crystallization (solid 2). The stages of crystallization at equilibrium of this liquid show that it evolves on the peritectic and produce olivine diogenite (Fig. 13, liquid 2). Olivines react with liquid at peritectic and are consumed partially or totally. When all the olivine has been consumed or isolated within the orthopyroxenes, the liquid leaves the peritectic to enter the liquid + orthopyroxene field (Fig. 13, liquid 3). The evolution of the liquid at the level of the peritectic and the subsequent passage through the “Opx + melt” field reflect the transition from equilibrium crystallization to fractional crystallization. We obtained olivine diogenite (solid 2) containing 3.4% olivine (Fe no. 30), 94% orthopyroxene (Fe no. = 74.86) and 2.3% spinel (Mg no.

39.21 and Cr no. 70.21) and traces of metal. This composition and the modal proportions of these minerals are very similar to those actually measured in NWA 4255. The results of our modeling suggest that NWA 4255 could be derived from the transition zone between the eucritic-diogenetic crust and the mantle of his parent body. These results are consistent with those of Mandler and Elkins-Tanton (2013).

**Outstanding issues**

The actual composition of spinel in NWA 4255 measured is Mg no. 15.3–22.4 and Cr no. 83.09–85.11, whereas the

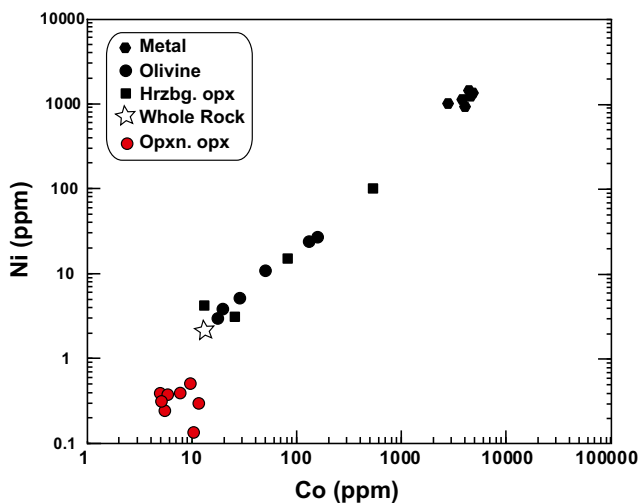


**Fig. 11** Ni vs. Co for olivine, orthopyroxene, metal and the whole-rock analyses of NWA 4255

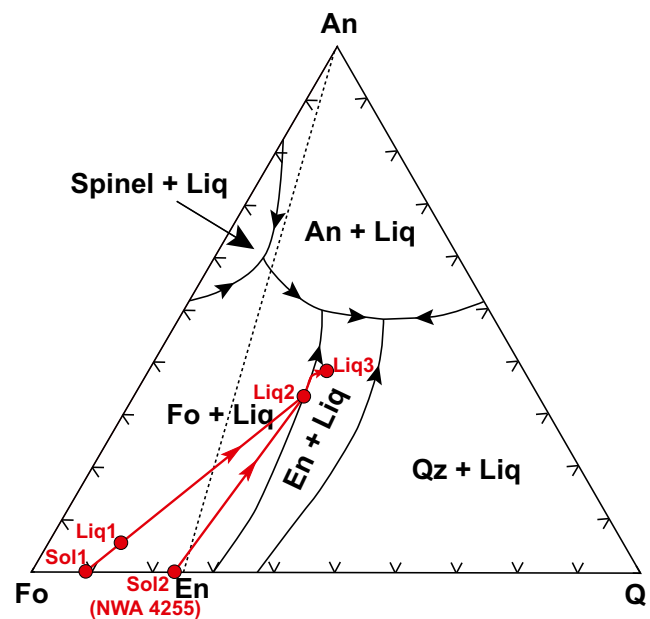


**Fig. 12** Data for NWA 4255 plotted in olivine-anorthite-quartz pseudoternary of Stolper (1975), showing how olivine diogenite formation can take place at the peritectic

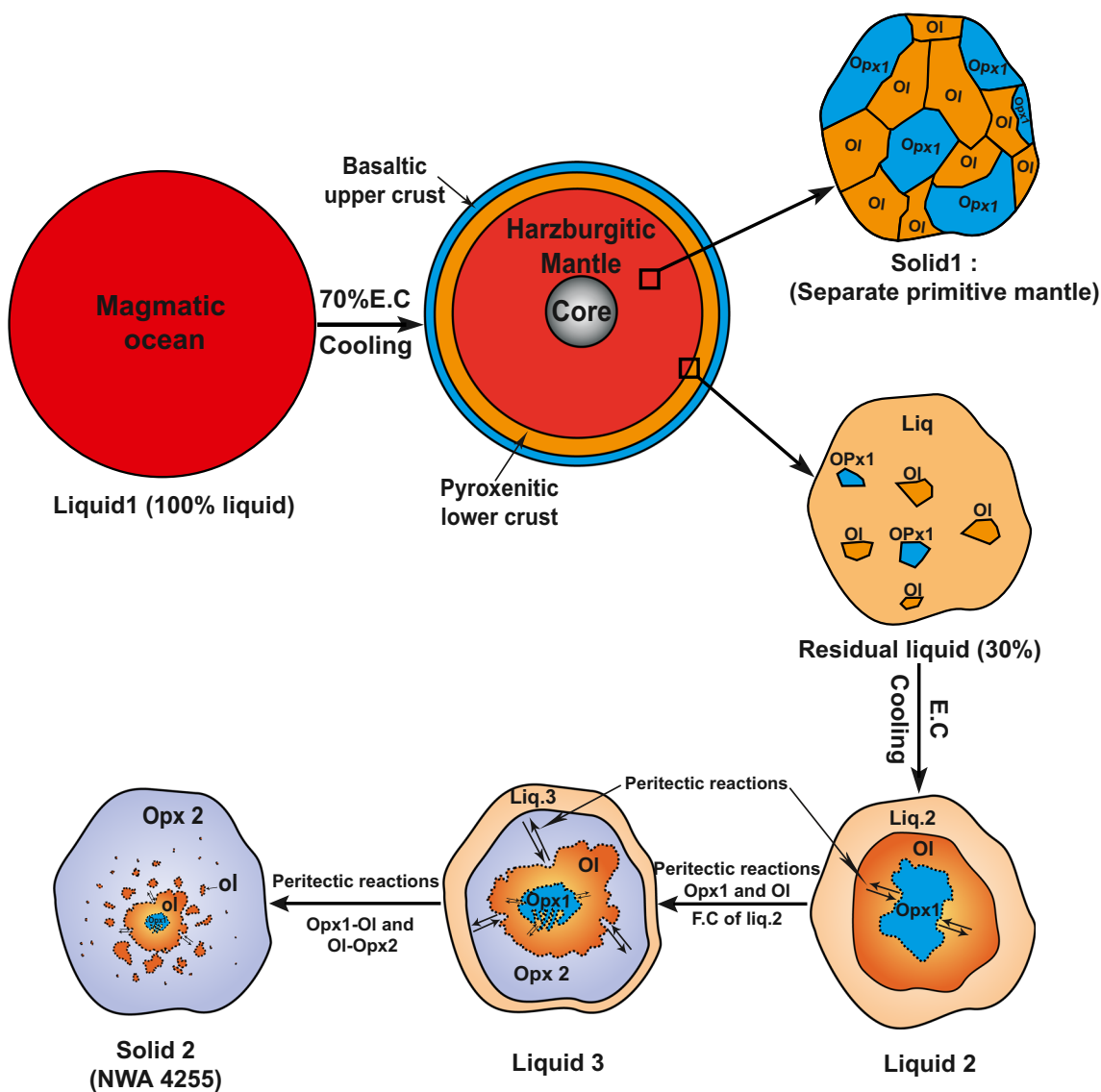


**Fig. 13** Schematic representation illustrating the proposed model for the genesis of the NWA 4255, starting from the differentiation and crystallization of a magma ocean. The schematic cross-section of a differentiated asteroid is based on that of Greenwood et al. (2015), using the

thicknesses of the various layers as given by a range of modeling studies of (Ruzicka et al. 1997; Righter and Drake 1997; Mandler and Elkins-Tanton 2013; Toplis et al. 2013). (See text for more details)

predicted values from the pMELTS calculations are (Mg no. 39.21 and Cr no. 70.21), which are significantly different. Thus, there is a problem in reproducing the magmatic composition of spinel, whereas there was no problem in reproducing this for the other silicates. According to the phase diagrams of basaltic systems at low pressure, there should be no spinel (Mg-Al spinel) at equilibrium, the spinel stability field being far from our compositions. However, the composition of the liquid particularly rich in Cr and Fe implies the Cr saturation and the chromium spinel precipitation (Irvine 1977). It is possible that the thermodynamic database of MELTS does not strictly cover these ranges of composition and fugacity oxygen to reproduce spinel composition.

Moreover, there are some differences between NWA 4255 and the others HEDs, such as the wide range of variation of the low concentration of Ni in the olivine. Therefore, the Ni/Co in olivine of NWA 4255 is much different from what is known in the literature, in addition to the low Fe/Mn ratio. At present, there is no simple explanation for these discrepancies.

### Conclusion

NWA 4255 displays two populations of orthopyroxene crystals as indicated by their major, minor, and trace element compositions. This distinction was also observed with respect to their texture. NWA 4255 is essentially composed of two

lithologies: one containing olivine, which we have termed a harzburgite, and the other an olivine-free orthopyroxenite. A transitional lithology is present at the contact between these two main lithologies. This olivine diogenite is an extraction in transitional zone between two different lithologies from Vesta, and it has undergone a subsequent brecciation.

Based on the petrographic observations and using chemical data for the modeling, we conclude that the two lithologies are genetically linked.

Based on the results of our modeling studies, Vesta evolved first via the formation of a primitive harzburgitic mantle. As soon as this unit was formed, it was separated from the liquid by a fractional crystallization process. The remaining liquid continued to crystallize along the peritectic to form olivine diogenites and then evolved further to form the diogenite by the fractional crystallization.

Finally, the harzburgitic and the orthopyroxenitic lithology are formed by the equilibrium crystallization (E.C) and the fractional crystallization (F.C), respectively. The NWA 4255 reflects transition between two different major magmatic processes in 4Vesta (E.C and F.C). The peritectic reactions are the link between these two processes. These lithologies come from the deepest zones of the crust, at the interface with the mantle.

**Acknowledgments** We thank Madame Marguerite Godard, for having analyzed one of the aliquots of the whole-rock traces at the Montpellier University. Thanks to J-L. Devidal for the assistance during the microprobe and the ICP-MS analysis. Thanks to J. Chevet for following the analyses of the whole rock. Thanks to J-M. Henot for making the mosaic images and M. Benbakkar for performing the ICP-AES analysis. Special thanks are extended to Magmas et Volcans Laboratory (Saint-Etienne, France) for the preparation of the samples for all analyses and also for welcoming into this laboratory to realize this work.

**Funding information** The Ministry of Higher Education and Scientific Research Algeria (M.E.S.R.S.) granted a PROFAS B+ grant to carry out this work in the Algerian-French program of doctoral scholarships, bilateral cooperation in the field of scientific research. Campus France financed part of the analyses of this work. Oxygen isotope studies at the Open University are funded by a consolidated grant from the Science and Technology Facilities Council (STFC), UK.

## References

- Anders E, Grevesse N (1989) Abundances of the elements: meteoritic and solar. *Geochim Cosmochim Acta* 53(1):197–214
- Barrat JA, Beck P, Bohn M, Cotten J, Gillet P, Greenwood RC, Franchi IA (2006) Petrology and geochemistry of the fine-grained, unbrecciated diogenite Northwest Africa 4215. *Meteorit Planet Sci* 41(7):1045–1057
- Beck AW, McSween HY (2008) Fe and Mn systematics in olivine-bearing diogenites. Abstract #1291, Lunar and Planetary Science XXXIX, USA
- Beck AW, McSween HY (2010) Diogenites as polymict breccias composed of orthopyroxenite and harzburgite: Diogenites as polymict breccias. *Meteorit Planet Sci* 45(5):850–872
- Beck AW, McSween HY, Bodnar RJ (2013) In situ laser ablation ICP-MS analyses of dimict diogenites: further evidence for harzburgitic and orthopyroxenitic lithologies. *Meteorit Planet Sci* 48(6):1050–1059
- Boesenberg JS, Delaney JS (1997) A model composition of the basaltic achondrite planetoid. *Geochim Cosmochim Acta* 61(15):3205–3225
- Bowman LE, Spilde MN, Papike JJ (1997) Automated energy dispersive spectrometer modal analysis applied to the diogenites. *Meteorit Planet Sci* 32(6):869–875
- Cartier C, Hammouda T, Doucelance R, Boyet M, Devidal JL, Moine B (2014) Experimental study of trace element partitioning between enstatite and melt in enstatite chondrites at low oxygen fugacities and 5GPa. *Geochim Cosmochim Acta* 130:167–187
- Drake MJ (2001) Presidential address: presented 2000 August 28, Chicago, Illinois, USA the eucrite/Vesta story. *Meteorit Planet Sci* 36(4):501–513
- Dreibus G, Wänke H (1980) The bulk composition of the Eucrite parent asteroid and its bearing on planetary evolution. *Z Naturforsch A* 35(2):204–216
- Fowler GW, Papike JJ, Spilde MN, Shearer CK (1994) Diogenites as asteroidal cumulates: insights from orthopyroxene major and minor element chemistry. *Geochim Cosmochim Acta* 58(18):3921–3929
- Fowler GW, Shearer CK, Papike JJ, Layne GD (1995) Diogenites as asteroidal cumulates: insights from orthopyroxene trace element chemistry. *Geochim Cosmochim Acta* 59(14):3071–3084
- Ghiorso MS, Hirschmann Marc M, Reiners Peter W, Kress VC III (2002) The pMELTS: a revision of MELTS aimed at improving calculation of phase relations and major element partitioning involved in partial melting of the mantle at pressures up to 3 GPa. *Geochem Geophys Geosyst* 3(5). <https://doi.org/10.1029/2001GC000217>
- Greenwood RC, Barrat JA, Scott ERD, Haack H, Buchanan PC, Franchi IA, Burbine TH (2015) Geochemistry and oxygen isotope composition of main-group pallasites and olivine-rich clasts in mesosiderites: Implications for the “Great Dunite Shortage” and HED-mesosiderite connection. *Geochim Cosmochim Acta* 169: 115–136
- Greenwood RC, Burbine TH, Miller MF, Franchi IA (2017) Melting and differentiation of early-formed asteroids: the perspective from high precision oxygen isotope studies. *Chem Erde-Geochem* 77:1–43
- Hahn TM, Lunning NG, McSween HY, Bodnar RJ, Taylor LA (2018) Mg-rich harzburgites from Vesta: mantle residua or cumulates from planetary differentiation? *Meteorit Planet Sci* 53(3):514–546
- Irvine TN (1977) Chrome spinel crystallization in the join  $Mg_2SiO_4$ - $CaMgSi_2O_6$ - $MgCr_2O_4$ - $SiO_2$ . *Carnegie Inst Washington Yearb* 76: 465–472
- Irving AJ, Kuehner SM, Carlson RW, Rumble D, Hupé AC, Hupé GM (2005) Petrology and multi-isotopic composition of olivine diogenite nwa 1877: a mantle peridotite in the proposed hedo group of meteorites. Abstract #2188 Lunar and Planetary Science XXXVI, USA
- Irving AJ, Bunch TE, Kuehner SM, Wittke JH, Rumble D (2009) Peridotites related to 4vesta: deep crustal igneous cumulates and mantle samples. Abstract #2466. 40th Lunar and Planetary Science Conference, USA
- Krawczynski MJ, Elkins-Tanton LT, Grove TL (2008) Krawczynski 2008. Petrology of mesosiderite(?) MIL03443,9; constraints on eucrite parent body bulk composition and magmatic processes. Abstract #1229, 39 th Lunar and Planetary Science Conference, USA
- Lodders K (2000) An oxygen isotope mixing model for the accretion and composition of rocky planets. In: Benz W, Kallenbach R, Lugmair GW (eds) From dust to terrestrial planets, vol 9. Springer Netherlands, Dordrecht, pp 341–354
- Lunning NG, McSween HY, Tenner TJ, Kita NT, Bodnar RJ (2015) Olivine and pyroxene from the mantle of asteroid 4 Vesta. *Earth Planet Sci Lett* 418:126–135

- Mandler BE, Elkins-Tanton LT (2013) The origin of eucrites, diogenites, and olivine diogenites: magma ocean crystallization and shallow magma chamber processes on Vesta. *Meteorit Planet Sci* 48(11):2333–2349
- Mayne RG, McSween HY, McCoy TJ, Gale A (2009) Petrology of the unbrecciated eucrites. *Geochim Cosmochim Acta* 73(3):794–819
- Miller MF (2002) Isotopic fractionation and the quantification of  $^{17}\text{O}$  anomalies in the oxygen three-isotope system: an appraisal and geochemical significance. *Geochim Cosmochim Acta* 66(11):1881–1889
- Miller MF, Franchi IA, Sexton AS, Pillinger CT (1999) High-precision  $\delta^{17}\text{O}$  isotope measurements of oxygen from silicates and other oxides: methods and applications. *Rapid Commun Mass Spectrom* 13:1211–1217
- Mittlefehldt DW (1994) The genesis of diogenites and HED parent body petrogenesis. *Geochim Cosmochim Acta* 58(5):1537–1552
- Mittlefehldt DW (2000) Petrology and geochemistry of the elephant moraine A79002 diogenite: a genomict breccia containing a magnesian harzburgite component. *Meteorit Planet Sci* 35(5):901–912
- Mittlefehldt DW (2015) Asteroid (4) Vesta: I. the howardite-eucrite-diogenite (HED) clan of meteorites. *Chem Erde-Geochem* 75(2):155–183
- Righter K, Drake MJ (1997) A magma ocean on Vesta: core formation and petrogenesis of eucrites and diogenites. *Meteorit Planet Sci* 32(6):929–944
- Ruzicka A, Snyder GA, Taylor LA (1997) Vesta as the howardite, eucrite and diogenite parent body: implications for the size of a core and for large-scale differentiation. *Meteorit Planet Sci* 32(6):825–840
- Sack RO, Ghiorso MS (1991) Chromian spinels as petrogenetic indicators: thermodynamics and petrological applications. *Am Mineral* 76:827–847
- Shearer CK, Fowler GW, Papike JJ (1997) Petrogenetic models for magmatism on the eucrite parent body: evidence from orthopyroxene in diogenites. *Meteorit Planet Sci* 32(6):877–889
- Shearer CK, Burger P, Papike JJ (2010) Petrogenetic relationships between diogenites and olivine diogenites: implications for magmatism on the HED parent body. *Geochim Cosmochim Acta* 74(16):4865–4880
- Stöpler E (1975) Petrogenesis of eucrite, howardite and diogenite meteorites. *Nature* 258:220–222
- Toplis MJ, Mizzon H, Monnereau M, Forni O, McSween HY, Mittlefehldt DW, Russell CT (2013) Chondritic models of 4 Vesta: implications for geochemical and geophysical properties. *Meteorit Planet Sci* 48(11):2300–2315
- Van Achterberg E, Ryan CG, Griffin WL (2001) GLITTER version 4 user's manual on-line interactive data reduction for the LA-ICP-MS microprobe. Macquarie Research Ltd, North Ryde 71 p